Received: 25 December 2019 | Revised: 1 February 2020 | Accepted: 11 February 2020

DOI: 10.1002/jbio.201960243

JOURNAL OF BIOPHOTONICS

FULL ARTICLE

# Efficient and cost-effective 3D cellular imaging by sub-voxel-resolving light-sheet add-on microscopy

**Fang Zhao[1] | Yicong Yang[1] | Yi Li[1,2] | Hao Jiang[1] | Xinlin Xie[1] | Tingting Yu[3] | Xuechun Wang[1] | Qing Liu[1] | Hao Zhang[1] | Haibo Jia[2] | Sheng Liu[4] | Mei Zhen[5] | Dan Zhu[3] | Shangbang Gao[2*] | Peng Fei[1*]**

[1]School of Optical and Electronic Information, Wuhan National Laboratory for Optoelectronics, Huazhong University of Science and Technology, Wuhan, China

[2]College of Life Science and Technology, Key Laboratory of Molecular Biophysics of the Ministry of Education, Huazhong University of Science and Technology, Wuhan, China

[3]Britton Chance Center for Biomedical Photonics, Wuhan National Laboratory for Optoelectronics, Huazhong University of Science and Technology, Wuhan, China

[4]School of Power and Mechanical Engineering, Wuhan University, Wuhan, China

[5]Department of Molecular Genetics, Lunenfeld-Tanenbaum Research Institute, Mount Sinai Hospital, University of Toronto, Toronto, Ontario, Canada

***Correspondence**
Peng Fei, School of Optical and Electronic Information, Wuhan National Laboratory for Optoelectronics, Huazhong University of Science and Technology, Wuhan 430074, China.
Email: feipeng@hust.edu.cn
Shangbang Gao, College of Life Science and Technology, Key Laboratory of Molecular Biophysics of the Ministry of Education, Huazhong University of Science and Technology, Wuhan, China
Email: sgao@hust.edu.cn

**Funding information**
Junior Thousand Talents Program of China; Innovation Fund of WNLO, The Fundamental Research Funds for the Central Universities, Grant/Award Numbers: 2019JYCXJJ012, 2019kfyRCPY060; Wuhan Morning Light Plan of Youth Science and Technology, Grant/Award Number: 2017050304010295; National Science Foundation of Hubei, Grant/Award Number: 2018CFA039; National Natural Science Foundation of China, Grant/Award Numbers: 31671052, 31871069, 61860206009, 21874052; Research Program of Shenzhen, Grant/Award Number: JCYJ20160429182424047; National Key R&D program of China, Grant/Award Number: 2017YFA0700501

## Abstract

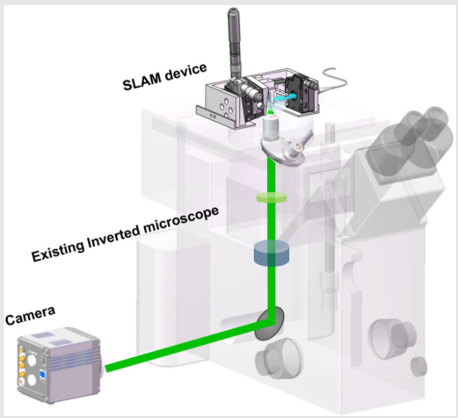


Light-sheet fluorescence microscopy (LSFM) allows volumetric live imaging at high-speed and with low photo-toxicity. Various LSFM modalities are commercially available, but their size and cost limit their access by the research community. A new method, termed sub-voxel-resolving (SVR) light-sheet add-on microscopy (SLAM), is presented to enable fast, resolution-enhanced light-sheet fluorescence imaging from a conventional wide-field microscope. This method contains two components: a miniature add-on device to regular wide-field microscopes, which contains a horizontal laser light-sheet illumination path to confine fluorophore excitation at the vicinity of the focal plane for optical sectioning; an off-axis scanning strategy and a SVR algorithm that utilizes sub-voxel spatial shifts to reconstruct the image volume that results in a twofold increase in resolution. SLAM method has been applied to observe the muscle activity change of crawling *C. elegans*, the heartbeat of developing zebrafish embryo, and the neural anatomy of cleared mouse brains, at high spatiotemporal resolution. It provides an efficient and cost-effective solution to

Fang Zhao, Yicong Yang, Yi Li, and Hao Jiang, contributed equally to this work.

convert the vast number of in-service microscopes for fast 3D live imaging with voxel-super-resolved capability.

**KEYWORDS**

3D imaging, add-on device, light-sheet microscopy, open source, voxel super-resolution

## 1 | INTRODUCTION

Light-sheet fluorescence microscopy (LSFM) has recently emerged as an imaging technique of choice for life science research [1–3]. With sharp plane illumination and orthogonal wide-field detection, LSFM allows rapid three-dimensional imaging of live samples with high axial resolution and low photo-toxicity [2–7]. Variants of LSFM, such as selective plane illumination microscopy (SPIM), multi-directional SPIM (mSPIM), ultramicroscopy, digitally scanned light-sheet microscopy, and Bessel plane illumination microscopy, have been developed in the past decade to increase the image resolution and expand imaging capacity from single cells to an entire cleared mouse [3, 7–19]. However, conventional LSFM modalities are often complicated and require special sample mounting, thus restricting their accessibility by general researcher community [2, 15, 20–22]. Several user-friendly LSFM methods, such as lattice microscopy [9], diSPIM [6, 23], and OTLS [24, 25], are recently developed to turn the light-sheet microscopy vertically, permitting laterally unconstrained imaging of samples commonly prepared on slides. By using an inverted 45° design, OTLS further allows for high-throughput imaging of samples immersed in a multi-well plate or microfluidic chip. Meanwhile, compact LSFM systems, for example, Open-SPIM, are also invented with simplified structures and reduced cost, disseminating advanced biological imaging for less-funded environments [26, 27].

Despite the abovementioned variations, all LSFM modalities operate on a fundamentally similar platform: a separate laser light-sheet illumination path, and wide-field detection system. Therefore, existing wide-field microscopes can be retrofitted for LSFM by adopting the light-sheet illumination source. Given the number of wide-field epifluorescence microscopes in service, upgrading existing microscopes for light-sheet illumination should be the simplest and most economical approach for most researchers to access LSFM imaging. Fluid-based LSFM methods use capillary or chip to drive the sample flow through a Gaussian laser light-sheet [28–33]. On a portable optofluidic platform, this class of methods can achieve LSFM imaging of certain types of flowing samples on conventional microscope. Attachable devices, such as Mizartilt, have been made to provide tilted light-sheet illumination to inverted microscopes. However, with fixed thickness and confocal range, the geometry of such tilted light-sheet is only suitable for imaging small samples at high magnification. But at this range, epifluorescence microscopes can already achieve thin optical sectioning capability [34].

Our previous development of a compact plane illumination device, which contains a tunable laser light-sheet illumination and sample mounting units [35], has rendered a simple and versatile tool to implement LSFM imaging on inverted microscope. Replacing the illumination system of the host microscope with a compact plane illumination path, the horizontal light-sheet laser selectively illuminates and excites fluorophores within thin focal planes, allowing the existing detection system to rapidly generate high-contrast fluorescence images. High-speed recording of consecutively illuminated planes then enables dynamics volumetric imaging of live specimens. In addition to converting a conventional wide-field microscope into a light-sheet microscope, we further integrate an off-detection-axis scanning scheme and a sub-voxel-resolving (SVR) algorithm that can three-dimensionally improves image resolution [36, 37]. Together, this sub-voxel-resolving light-sheet add-on microscopy method (SLAM) we herein report enables conventional fluorescence microscopes to perform resolution-enhanced volumetric imaging from small or large samples. Using GPU-based computation, SLAM can further increase the throughput of image reconstruction and analysis.

We applied SLAM to image samples of a wide range of sizes, from the tiny behaving *C. elegans* larva, the beating zebrafish heart, the vessel system of entire zebrafish embryo, to the cleared mouse brains. Compared with the performance of the host microscope, SLAM provides over 10-fold enhanced resolution and a capacity for 3D imaging at up to three volumes per second. We also show that such a temporal and spatial resolution is sufficient for quantitative analyses on the cardiovascular dynamics, vessel formation, and motor activity output.

## 2 | RESULTS

### 2.1 | The design and operation of SLAM

Sub-voxel-resolving light-sheet add-on microscopy method includes a portable add-on device mounted to the

microscope and an algorithm for processing acquired images. The device consists of following components: a collimated fiber-coupled laser as the illumination source, a cylindrical lens with an adjustable slit to generate geometry-tunable laser light-sheet, a sample-handling unit that includes a magnetic holder to mount and place samples in close proximity to the objective, a glass chamber to immerse samples in index-matched liquid, and a tilt stage with a motorized actuator to scan samples at off-$z$-axis direction (Figure 1A; Figure S2). All components are assembled in an aluminum base that is currently designed to be compatible with Olympus

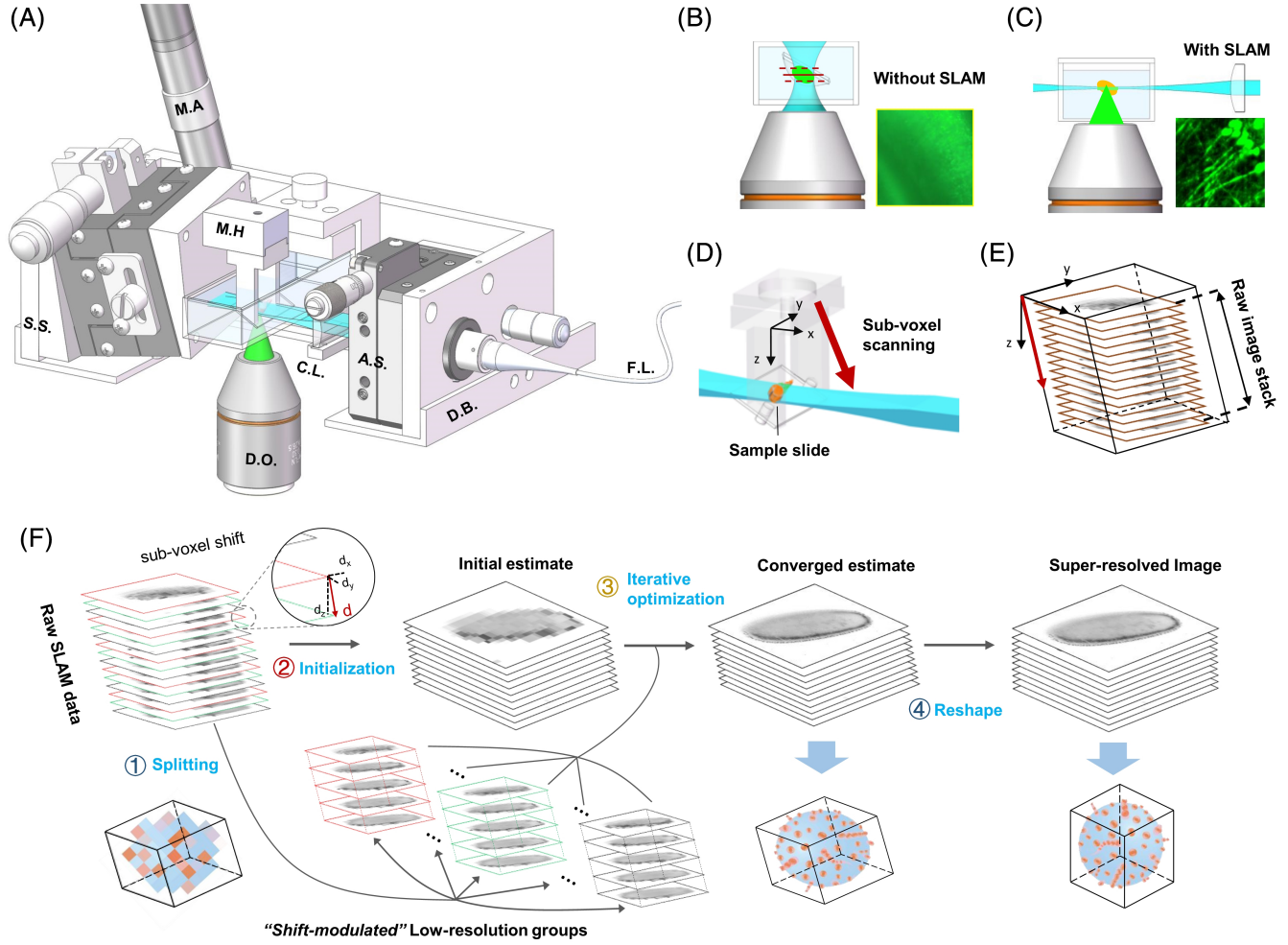


**FIGURE 1** Schematic of the sub-voxel-resolving light-sheet add-on microscopy (SLAM). A, The structure of the add-on device, consisting of several compact mechanical parts and small optical elements on a device base (D.B.). The major components include: a collimated fiber-coupled laser (F.L.) as the illumination source; a cylindrical lens (C.L.) combined with an adjustable slit (A.S.) for generation of tunable laser light-sheet; a magnetic holder (M.H.) for placing the sample close to the detection objective (D.O.); a glass chamber (G.C.) for housing the sample into an index-matched liquid environment; and a sloped stage (S.S.) driven by a motorized actuator (M.A.) for scanning the sample through the light-sheet along a direction off-$z$-axis. B, Conventional microscope's epi-illumination. C, In-focused plane illumination. D, For 3D imaging, the sample is first mounted on a transparent fluorinated ethylene propylene (FEP) plate using 0.5% hydrogel. Then, via a magnet adapter, the plate is firmly immersed into a liquid-filled chamber, with an angle of 30° to the horizontal plane. E, Sub-voxel scanning off the $z$-axis. The sample is scanned through the laser light-sheet along a direction 10° to 20° off the $z$-axis, while the microscope's detection system simultaneously collects the planar-excited fluorescent signals using a high-speed camera. The step-size is set much smaller than the light-sheet thickness. This scheme generates a stack of raw images encoded with spatial shifts beyond the native solution. F, Sub-voxel-resolving (SVR) reconstruction of acquired raw data. First, according to Nyquist sampling theorem, the raw image stack is separated into several LR stacks along $z$-axis. With sub-voxel scanning, each LR image stack not only presents native system resolution, but also carries 3D, sub-voxel information that cannot be resolved in raw data (step 1). Following the reversion of image degradation process in spatial domain, these LR images are imported into the SVR computation procedure to iteratively solve a voxel-super-resolved estimate, which resolves structural details beyond the limit of system optics (steps 2 and 3). Lastly, a voxel realignment is applied to the SVR estimate to correct the shape deformation introduced by sub-voxel scanning (step 4)

IX73, and can be easily adjusted to fit other models (Figure S2).

Through the truncation of incident Gaussian beam using the slit, the illumination unit generates a horizontal laser light-sheet with tunable axial extent of sectioning (~5-15 μm). Replacing the wide-field illumination of the host microscope, it restricts excitation at the vicinity of objective lens' focal plane (Figure 1A). Fluorescent signals emitted from the illuminated planes are collected via the original optical path of the host microscope (Figure S1). Together, they effectively transform wide-field epifluorescence imaging (Figure 1B) to in-focused, light-sheet fluorescence imaging (Figure 1C). As shown in vignettes (Figure 1B,C), due to reduced out-of-focus excitation, unprocessed images acquired from SLAM already exhibit improved contrast.

In the sample-handling unit, a motorized actuator (Z812B, Thorlabs; Table S1) moves the sample through a stationary light-sheet either continuously or with discrete step-size. This stage includes a customized tilting plate that makes the actuator's scanning axis oblique to the light-sheet. Typically, SLAM scans samples at ~70° to 80° angles with respect to the x and y dimension of the camera pixel grid (Figure 1D,E), and the microscope detects fluorescent signals plane by plane with an ultra-fine step-size (Figure 1E). This unconventional off-$z$-axis scanning mode at small step d allows unprocessed SLAM image sequences to encrypt both lateral and axial shifts ($d_x$, $d_y$, and $d_z$). These spatial shifts are modeled in the subsequent SVR computation to generate output images with improved resolution. See Supporting Information for the complete part list (Table S1), part pictures (Figure S2), CAD drawing (Figure S3), and assembly animation (Video S1) for the add-on device.

## 2.2 | The SVR reconstruction of acquired images

Unprocessed SLAM images already show significant improvement in contrast and axial resolution to those obtained by the host microscope due to plane illumination. A SVR reconstruction of the SLAM image stacks further increases the system space-bandwidth-product (SBP), the number of degrees of freedom that an optical system can extract from a signal [38].

Our SVR procedure is carried out as follows. The raw, over-sampled SLAM image sequence is first subdivided into a number of low-resolution (LR) image stacks by appropriate resampling rate (Figure 1F, step 1). Each segmented image stack presents standard resolutions simply accepted from the optics combination of plane illumination unit (axial) and inverted microscope (lateral). Thus, each LR stack can be considered as a regular SPIM result that contains sub-voxel resolution, 3D shifts relative to all other LR stacks. From these LR measurements, a SVR computation procedure is developed to model their spatial correlation, and applied iteratively to obtain high-resolution (HR) output across a large image volume (Figure S6) [33]. In practice, HR output is achieved via minimizing the following cost function.

$$\widehat{\underline{I}} = \underline{I}\mathrm{ArgMin}\left[\sum_{k=1}^{N}\rho(P_k, D_k O_k S_k \underline{P}) + \lambda\Upsilon(\underline{I})\right] \quad (1)$$

where $P_k$ is the $K$th LR measurement, and $D_k$, $O_k$, $S_k$ represent the down sampling, blurring, and sub-voxel shifting operations, which simulate the camera digitalization, optical imaging, and off-$z$-axis scanning in the real light-sheet imaging process, respectively. The equation iteratively seeks a final HR solution, which has the maximum likelihood (evaluated by $\rho$ and regularized by $\Upsilon$) to LR measurements after the aforementioned degradation operations being successively applied to it (Figure 1F, steps 2 and 3). A voxel re-alignment is applied at the final step to recover an accurate reconstruction of the sample from the slight deformation induced by the off-$z$-axis scanning procedure (Figure 1F, step 4). We first validate the efficiency of SVR using simulated images (Figure S7), and demonstrate below that SLAM-SVR provides a simple, cost-effective, and powerful tool for HR mapping of various biological samples.

To verify that our method has a high time throughput, we compared the image acquisition speed and calculation speed of SLAM-SVR (0.03 NA illumination and 4×/0.16 detection) and 20× SLAM (0.066 NA illumination and 20×/0.4 detection). We use a 3.3 × 3.3 × 2 mm brain tissue as our imaging sample to calculate the imaging time and calculation time in two modes. The results are compared in Table S3.

## 2.3 | SLAM-based LSFM imaging under different modes

Sub-voxel-resolving light-sheet add-on microscopy method is designed to have the capacity to image samples of a large size range. By tuning the slit width (typically between 6 and 1 mm) and truncating the incident Gaussian beam, the illuminating NA for generating the light-sheet could vary from ~0.066 to 0.02. The geometry of laser light-sheet is then experimentally measured with its confocal range adjustable from hundreds of microns to millimeters, and center thickness from ~5 to 15 μm (Figure S4). The tunable light-sheet illumination, together with multiple

objectives of the host microscope, makes highly flexible SLAM imaging for biological samples of a large size range (illustrated in Figure 2).

Using fluorescent beads (~200 nm in diameter) as the point source, we assessed and compared the performance of five imaging modes: the 4× epifluorescence mode (4×/0.16 objective illumination and detection) on a conventional microscope, the 4× SLAM mode (0.03 NA illumination +4×/0.16 detection), the 4× SLAM-SVR mode, the 10× SLAM mode (0.066 NA illumination +10×/0.4 detection), and the 20× SLAM mode (0.066 NA illumination +20×/0.45 detection) on a SLAM-enabled conventional

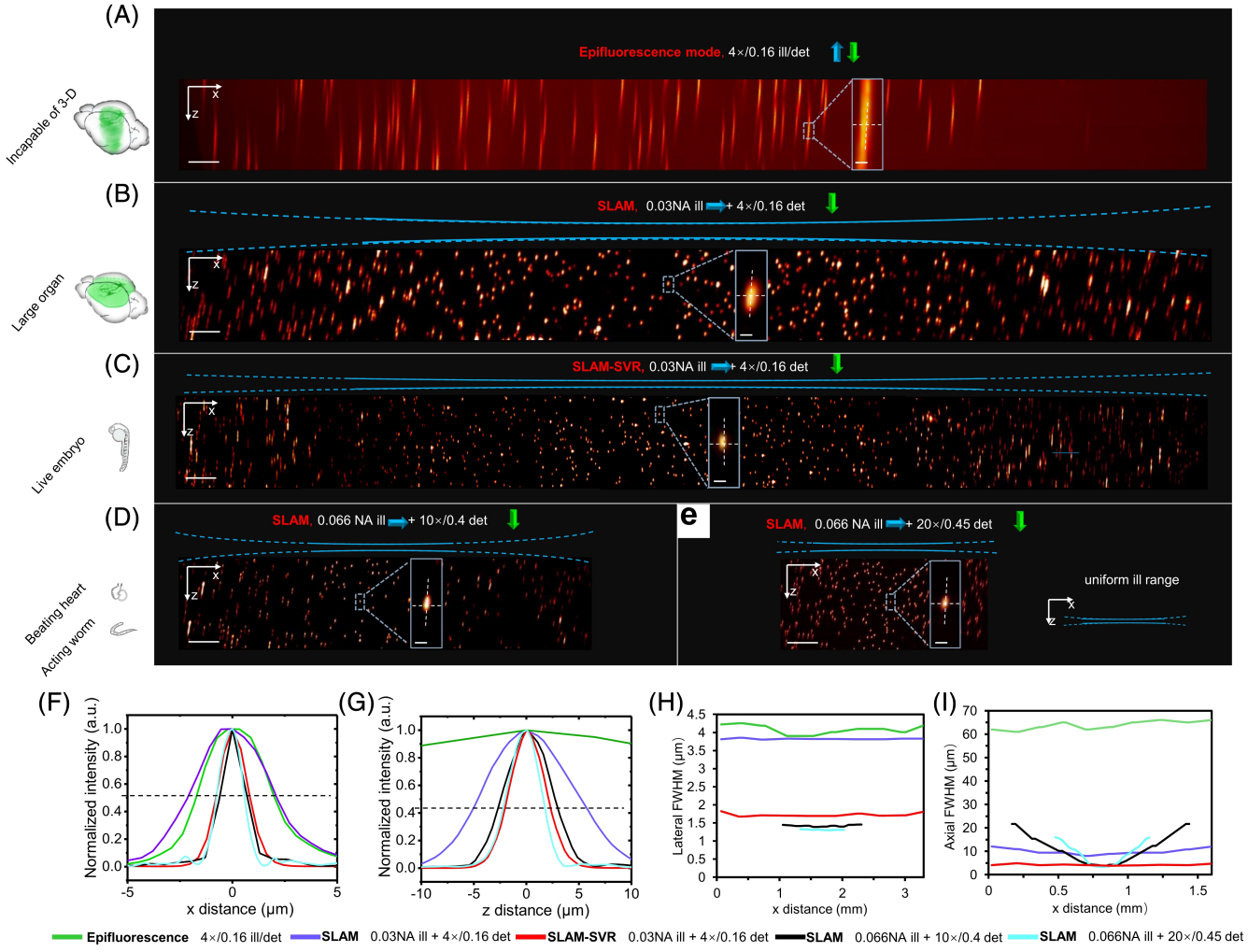


**FIGURE 2** Characterization of SLAM imaging. The *x-z* point spread function (PSF) images of fluorescent beads (~200 nm) acquired by five imaging modes: A, the conventional 4× epifluorescence mode (4×/0.16 NA illumination/detection); B, the 4× SLAM mode (0.03 NA illumination +4×/0.16 detection); C, the 4× SLAM-SVR mode (0.03 NA illumination +4×/0.16 NA detection); D, the 10× SLAM mode (0.066 NA illumination +10×/0.4 NA detection); E, the 20× SLAM mode (0.066 NA illumination +20×/0.45 NA detection). By analyzing the axial extents and lateral distributions of the PSF of these images, we determine properties of the plane illumination under each mode. The confinement of axial sectioning, which is a key determinant of the axial resolution, and the confocal range, within which the axial extents of resolved beads are relatively uniform, are illustrated as blue line drawings. Geometries of these tunable light-sheets generally comply with the law of hyperbolic focused Gaussian beam, except the one from 4× SLAM-SVR, which maintains a wide plane illumination range by 0.03 illuminating NA but computationally narrows it axial extent by a factor of 2.5. F and G, Linecuts (as shown in insets in A-E) through the central beads for each method, with 50% intensity level (dashed line) shown for estimation of the FWHM. After SVR reconstruction, the FWHMs of PSF by 4× SLAM are improved from ~4 μm/10 μm to ~1.7 μm/4 μm, which are not only far better than the measurements by original wide-field microscope (~4 μm/60 μm), but also comparable to 10× and 20× SLAM (~1.4 μm/5 μm, and ~1.3 μm/4 μm) with higher N.A. configurations. Scale bars are 100 μm in (A) to (E), and 5 μm in insets. H and I, The lateral and axial PSF variations across the FOV (*x* direction) of the five imaging modes in (A) to (E) (15 beads measured for each group), verifying the superior plane illumination across large-FOV and at high resolution by 4× SLAM-SVR. FWHM, full width at half-maximum; SLAM, sub-voxel-resolving light-sheet add-on microscopy; SVR, sub-voxel-resolving

microscope. Figure 2A-E shows the *x-z* point spread function (PSF) images measured by five modes, and Figure 2F, G shows the intensity plots of lines through the resolved beads (insets in A-E). The full width at half-maximum values (FWHMs) of these plots indicated the lateral and axial resolving powers of these modes. Compared to the wide-field mode, the addition of plane illumination alone enhanced the axial resolution by ~sixfold, shown as >60 μm for 4× epifluorescence versus ~10 μm for 4× SLAM. When SVR computation was applied, the 4× SLAM-SVR mode further improved the resolution from ~4 μm/10 μm to ~1.7 μm/4 μm. Note that the latter reached similar resolving powers as the 10× and 20× SLAM (~1.4 μm/5 μm and ~1.3 μm/4 μm), respectively. Note that the light-sheet illumination maintains a wide confocal range (Figure 2B,C, blue drawings), within which the axial resolution of resolved beads are relatively uniform. Consistent with the law of hyperbolic Gaussian light-sheet, this uniform illumination range of 4× SLAM is measured ~5 times longer than those of 10× and 20× SLAM with the 0.066 illuminating NA (Figure 2C-E, blue drawings). This results in a large imaging FOV while achieving similar resolution. Therefore, as SLAM imaging has enhanced the conventional epifluorescence microscope with better axial resolution and higher contrast, SLAM-SVR further expands the imaging capability of large organisms, such as whole zebrafish embryo (Figure 4) and thick mouse brain tissues (Figure 5), at high throughput.

## 2.4 | High-speed, dual-color SLAM imaging of the beating zebrafish embryo heart

To examine SLAM's temporal resolution, we first performed dual-color imaging of the heart of a zebrafish embryo to resolve its cardiac hemodynamics. Transgenic zebrafish embryos with the myocardium and red blood cells labeled with GFP and DsRed, respectively, were subjected to SLAM imaging with the 10× SLAM mode as described above. Consecutive frames of beating myocardium (*cmlc*:*GFP*) and flowing red blood cells (RBCs, *gata1*:*DsRed*) were simultaneously recorded using a beam splitter (Hamamatsu W-VIEW GEMINI) and superimposed afterward to visualize the cardiac hemodynamics. For comparison, we acquired images of heart beating in one cardiac cycle using the epi-illumination mode.

As shown in Figure 3C, the epifluorescence image series (at 90 ms interval) were blurry, incapable of demarcating cardiac structures. When the same sample was observed under 10× SLAM mode, the plane illumination significantly improved the contrast and sharpness. Two selectively illuminated planes of the heart were imaged at high spatial resolution, revealing the dynamic changes in the endo, epicardial boundaries and blood pumping (Figure 3A,B and Figure S8; Video S2).

Follow-up studies on cardiac hemodynamics were also enabled because of the improved visualization. We first segmented the dynamic boundaries of the beating heart and used computational fluid dynamics (CFD) analysis to compute its time-variant strain rate (Figures S8 and S9) [39, 40]. The strain rate variation of beating ventricle (Figure 3D) is consistent with the periodic diastole and systole stages of heat beating. These images are also of sufficient quality to allow CFD estimation of the inflow/outflow velocities by the amount of pumped RBCs (Figure 3E), and transient pressures at the inner surface (Figure 3F). From these images, we analyzed the continuous pressure change in one complete cardiac cycle (Figure S9 and Video S3).

## 2.5 | SLAM imaging and analysis of an entire zebrafish embryo

We next tested SLAM's capacity to image entire developing zebrafish embryo. A 72 hpf zebrafish embryo with its endothelium labeled with GFP (*Tg fli1*:*EGFP*) was imaged using the 4× SLAM-SVR mode. The reconstructed 3D blood vessels across the entire embryo encompassed 10 gigavoxels (Figure 4A), where small structures, such as the subintestinal veins were observable (Figure 4B).

We compared the same structure imaged by the 4× SLAM (Figure 4C), 10× SLAM (Figure 4D), and epifluorescence (Figure 4E) mode, respectively (see Table S2 for imaging parameters). 4× SLAM showed improved image quality (Figure 4C) as compared to the epifluorescence imaging (Figure 4E), whereas 4× SLAM-SVR further broke the SBP limit of the 4× optics, reconstructing finer cellular details visible at global scale (Figure 4B). In this mode, different vessel structures across the embryo, such as mesencephalic vein (Msv), central artery (CtA), intersegmental vein (IsV), and so on, are all clearly identified, accurately segmented, and readily quantifiable (Figure 4F). Lastly, we compared the performance of SLAM with a SPIM (self-assembled) and a confocal microscope (Olympus FV3000). Images acquired by SLAM showed comparable quality with those acquired by the benchtop SPIM and confocal microscope (Figure S10).

## 2.6 | High-throughput mapping of cleared mouse brain by SLAM

We three-dimensionally mapped a half mouse brain (~7.3 × 3.5 × 5.5 mm) at single-cell resolution quickly in

10 minutes, demonstrating the success of SLAM for large samples. A half brain (~7.3 × 3.5 × 5.5 mm) of a 8-week-old transgenic mouse where neurons were labeled by GFP (Tg:thy1-GFP-M) was optically cleared by uDISCO [41] (Figure 5A, insets). Cleared brain was then imaged by SLAM-SVR with a large-FOV setup (0.02 NA illumination and 4×/0.16 detection). Due to the large-FOV, only two stitching was required to generate three overlapping stacks, each containing 9000 frames acquired in ~3 minutes. The sub-voxel acquisition exhibited a low photobleaching due to its plane illumination mode and relatively short imaging time (Figure S11). Applying SVR and a tile stitching, we reconstructed the half brain with a super-resolved voxel size of 0.54 × 0.54 × 3 μm. Figure 5A shows the reconstructed volume rendering of the brain that encompasses 160 gigavoxels. Transverse planes at different depths (0.5-5 mm; Figure 5B) verified the high transparency of cleared brain and success of

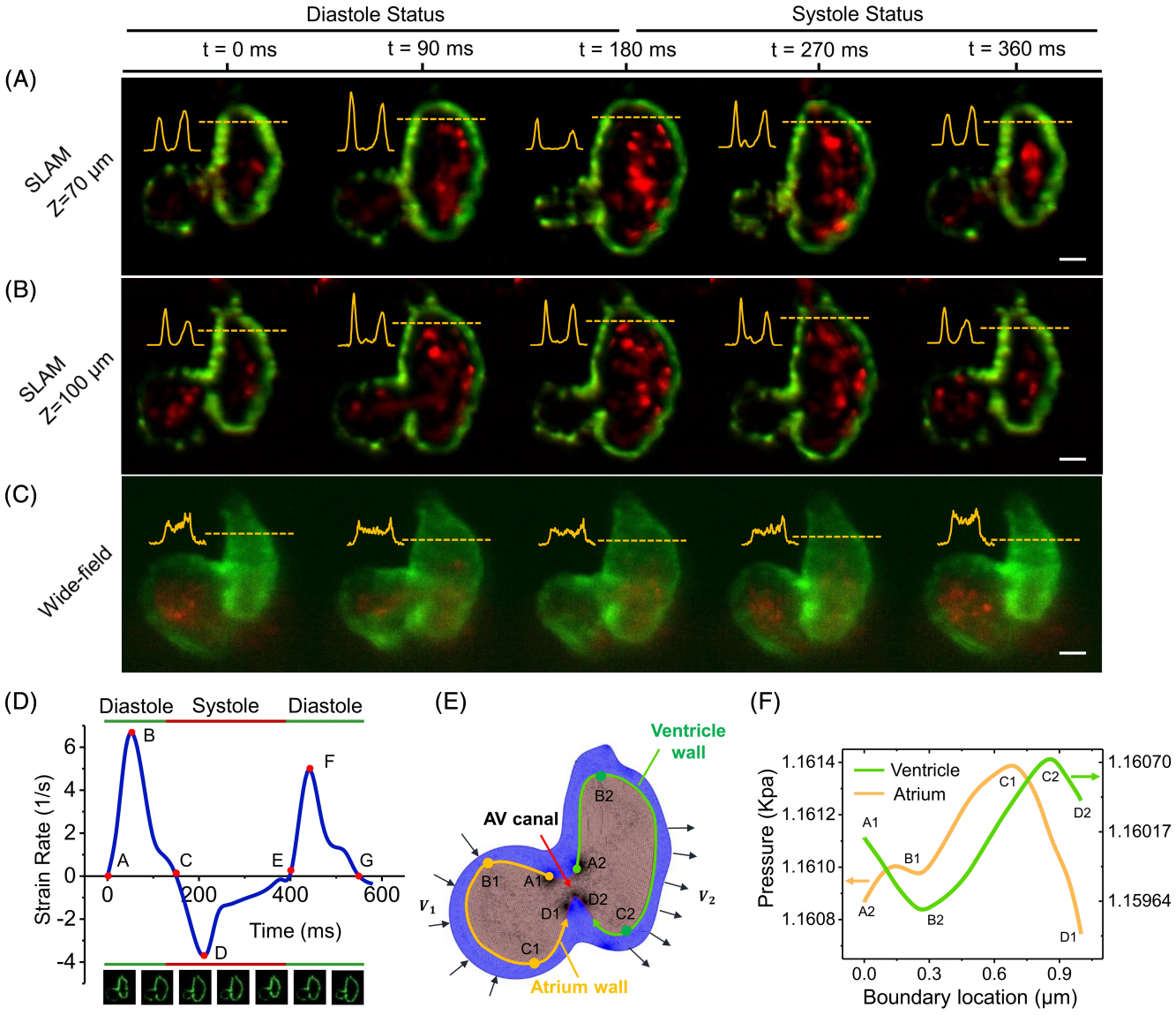


**FIGURE 3** Dual-color SLAM imaging of the beating heart of zebrafish embryo reveals fast cardiac hemodynamics. Through sharp optical sectioning by SLAM, high-contrast images from selective planes, 70 μm, A, and 100 μm, B, in *z* depth can be rapidly obtained at 100 fps. The consecutive images of beating myocardium (*cmlc*:*GFP*) and flowing red blood cells (RBCs, *gata1*:*DsRed*) are simultaneously recorded and merged to capture the cardiac hemodynamics. C, Heart images taken by the same conventional microscope without SLAM. The line profiles through the myocardial walls are plotted (yellow insets in A-C) to indicate the improvement of image contrast by SLAM. With clearly defined inner and outer boundaries of the beating heart in each image frame in (A) and (B), the strain rate of myocardium throughout one cardiac cycle is plotted and correlated with the state of heart beating cycle, D. E, Segmentation of a beating heart based on SLAM images. F, The pressure at different heart junctional boundaries. Scale bars are 50 μm in (A) to (C). SLAM, sub-voxel-resolving light-sheet add-on microscopy

deep tissue imaging. A 100-μm depth maximum-intensity-projection (MIP) at mid-brain (3 mm) (Figure 5C) further highlights the diverse morphologies of the massive amount of fluorescence-labeled neurons at different brain regions (hippocampus, cortex, and thalamus). Similar to the zebrafish studies, we compared the output of different SLAM imaging modes. SLAM alone significantly improved the contrast and resolution of the acquired images when

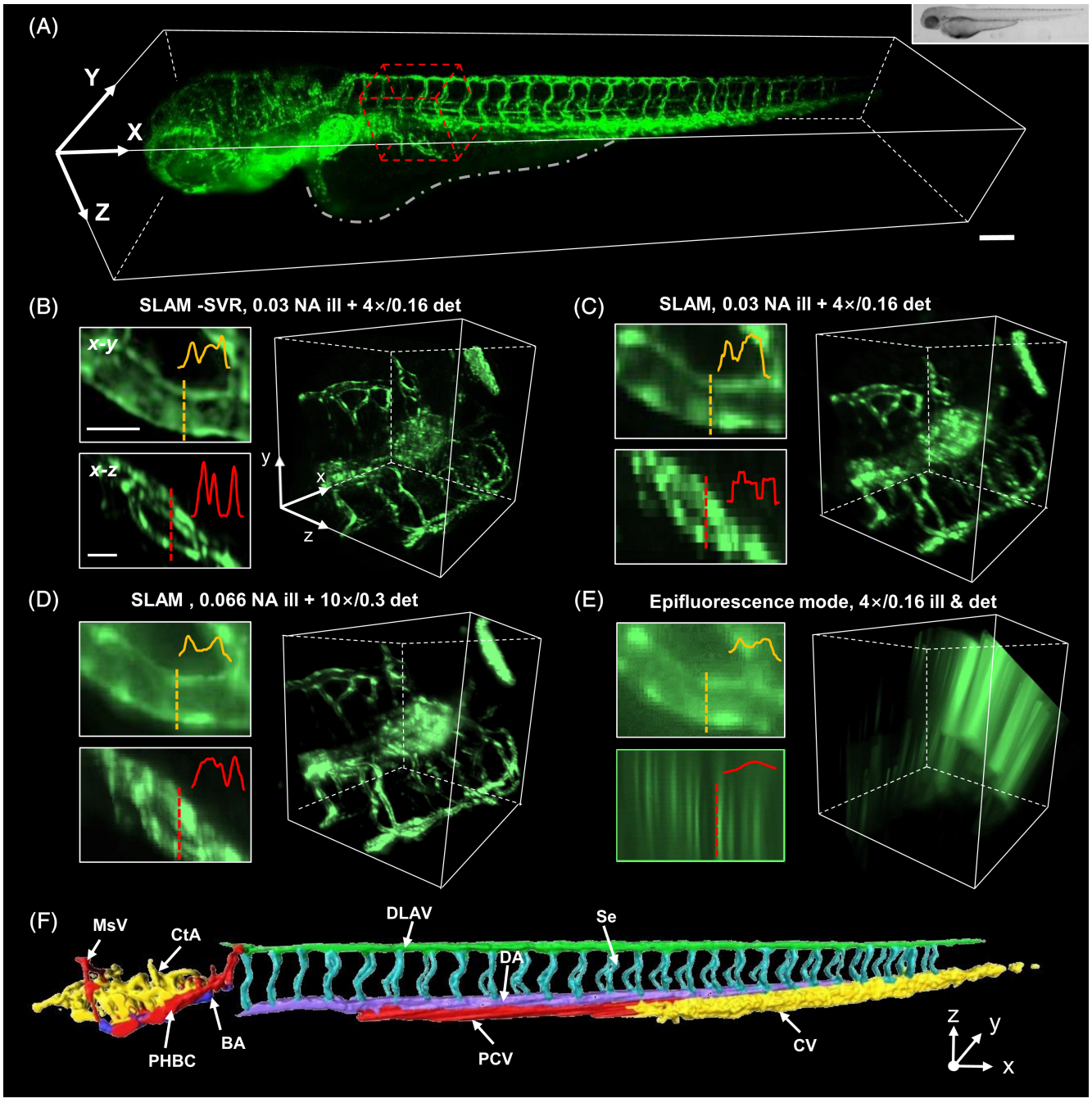


**FIGURE 4** 3D visualization and quantitative analysis of a whole zebrafish embryo using SLAM. A, A 72 hpf zebrafish embryo with GFP-labeled endothelium (*Tg fli1:EGFP*) is imaged by 4× SLAM-SVR mode. The reconstructed blood vessel system encompasses 10 gigavoxels after SVR computation. The resolved endothelium features of a subintestinal vein at the anterior part of the fish are shown in (B). C to E, Further compares the same structure imaged by the 4× SLAM, 10× SLAM, and epifluorescence mode, respectively. The line profiles through the resolved vessels are plotted (red and yellow insets in B-E), to indicate the achieved resolutions by each mode. Following image reconstruction, different vessel structures across the entire embryo, such as mesencephalic vein (Msv), central artery (CtA), and intersegmental vein (IsV), are shown in (F). Scale bars are 100 μm in (A), and 20 μm in (B) to (E). GFP, green fluorescent protein; SLAM, sub-voxel-resolving light-sheet add-on microscopy; SVR, sub-voxel-resolving

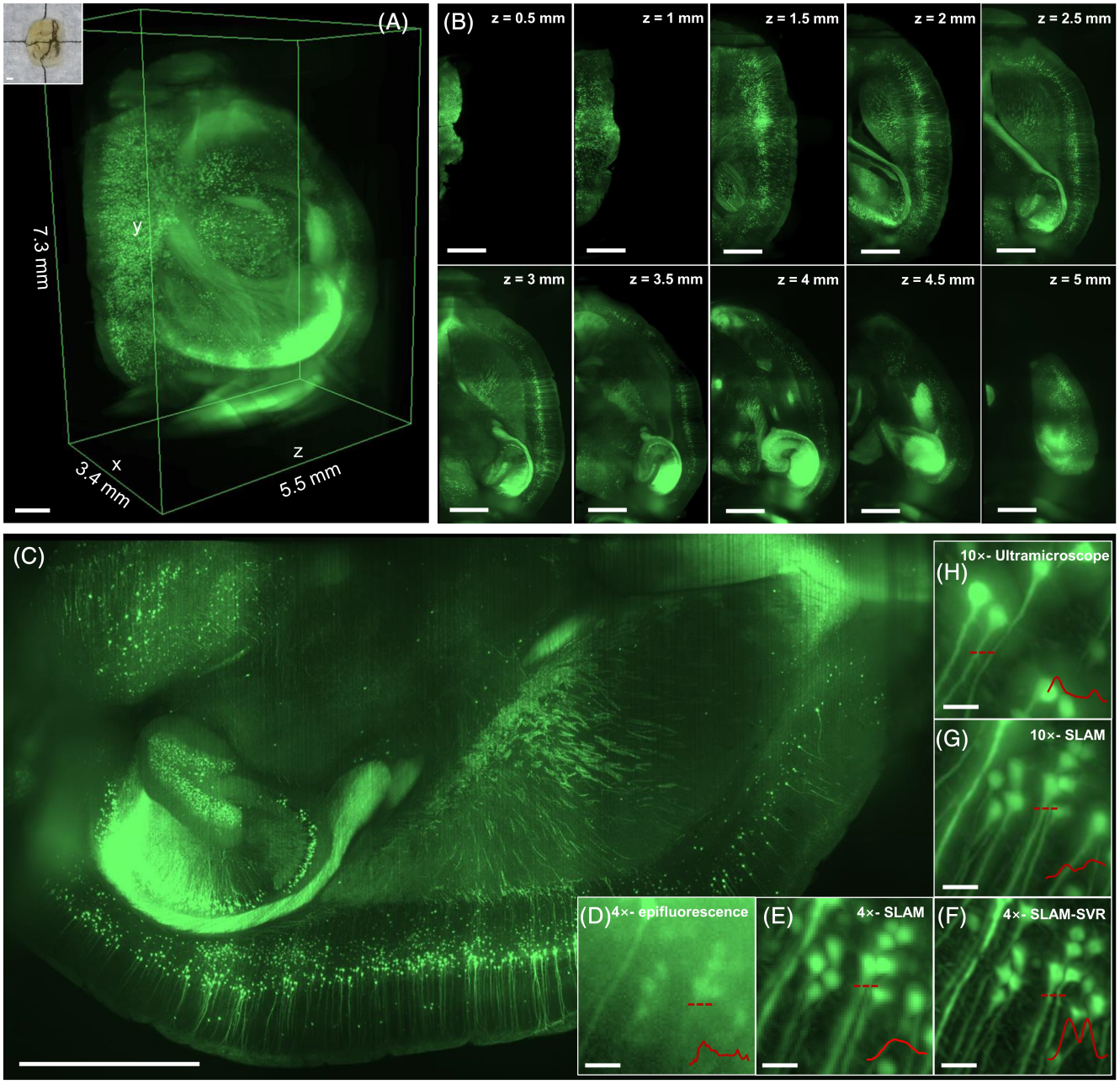


**FIGURE 5** Fast 3D mapping of the mouse brain by SLAM. A, A half mouse brain (8 weeks), with GFP-labeled neurons (Tg:thy1-GFP-M, inset) is cleared by uDISCO clearing (inset) and imaged by the 4× SLAM-SVR mode. The digital reconstruction of neurons in the half telencephalon results in 160 gigavoxels after SVR computation. B, The transverse MIPs (100-μm depth) of mouse brain from superficial ($z = 0.5$ mm) to deep ($z = 5$ mm) layers. Note that the image quality remains sharp at 5 mm in depth. C, Magnified view of the transverse plane at $z = 3$ mm depth. D to G, Compared high-resolution vignettes of a small cortex imaged by (D) the 4× epifluorescence mode; E, the 4× SLAM mode; F, 4× SLAM-SVR mode; G, 10× SLAM. H, An image of the same sample taken by an ultramicroscope (10× detection; ~10 μm plane illumination), which shows similar quality as in the 10× SLAM mode. The line profiles through the resolved neuronal fibers are plotted (red insets in D-H), to indicate the achieved resolutions by each mode. Scale bars are 1 mm (A-C) and 20 μm (D-H). GFP, green fluorescent protein; MIP, maximum-intensity-projection; SLAM, sub-voxel-resolving light-sheet add-on microscopy; SVR, sub-voxel-resolving

compared to those from the conventional epifluorescence imaging (Figure 5D). The densely packed neuronal fibers remain dim in unprocessed SLAM images due to the large-FOV setup (Figure 5E). Applying SVR computation (Figure 5F) significantly resolved the neuronal dendrites. The resolved image volume was comparable to that acquired at 10× SLAM without SVR, confirming the efficiency of the computation.

Lastly, we compared the output of SLAM with that of a benchtop Ultramicroscope I (LaVision Biotech, Germany), a light-sheet imaging modality for large samples. SLAM and Ultramicroscope could reach similar image quality at similar optical setups (10× detection, ~10 μm plane illumination; Figure 5G,H). The SLAM-SVR mode further allows imaging at 4×'s FOV to achieve 10×'s resolution. Thus, SLAM can be readily applied to imaging applications that require high spatial resolution across large volumes at high throughput.

## 2.7 | Rapid functional volumetric imaging of behaving *C. elegans* using SLAM

We applied SLAM to image muscular $Ca^{2+}$ activities of moving *C. elegans* in five dimensions (3D space + time + spectrum). A transgenic *C. elegans* larva (*Pmyo-3-GCaMP6s*::*Cherry*) that expresses a genetic calcium reporter GCaMP6::wCherry in its entire body wall muscles was imaged while animals were allowed to crawl in 1% agarose. We employed a configuration of 20×/0.45

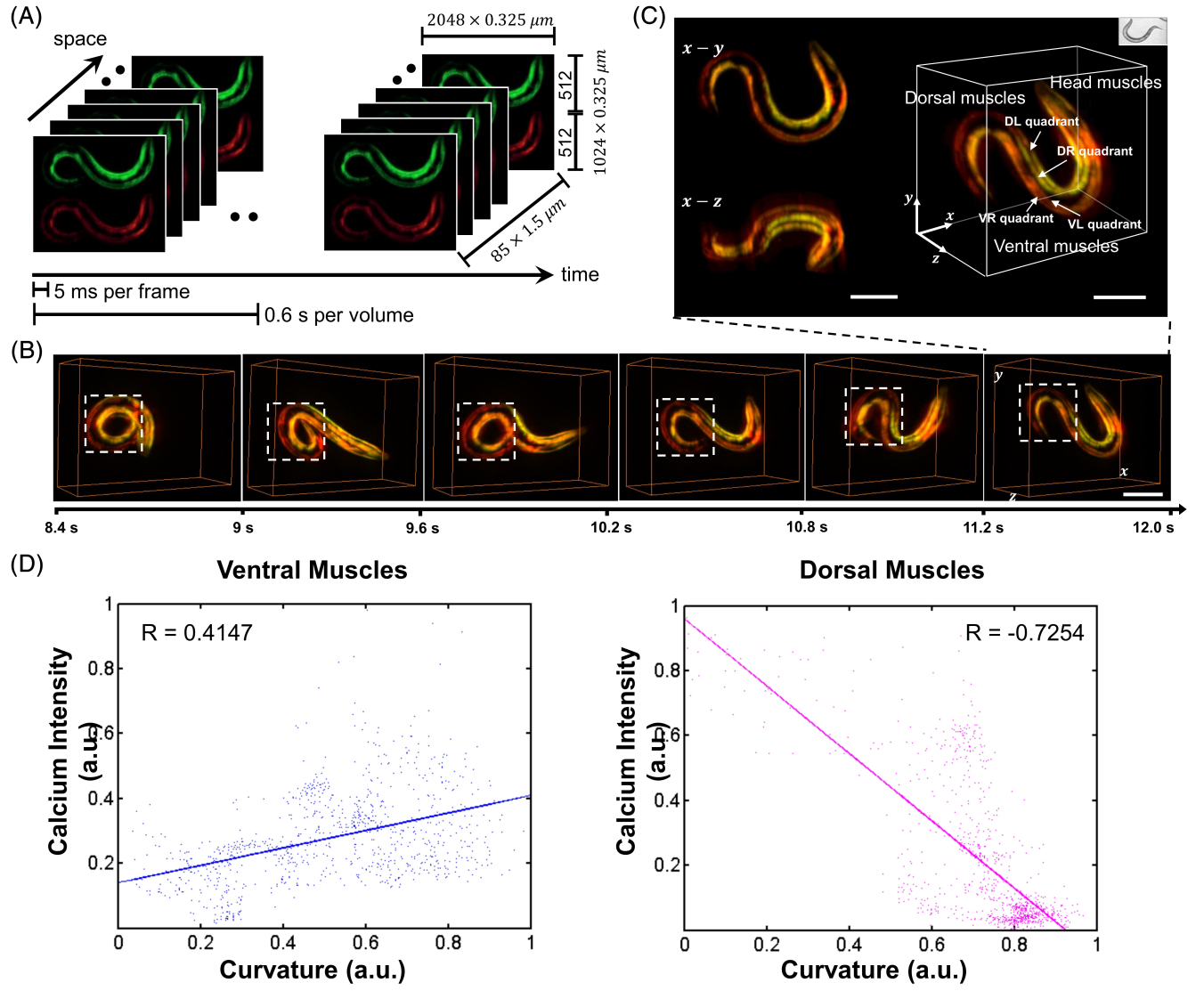


**FIGURE 6** Dual-channel SLAM imaging of muscular activities of behaving *C. elegans* larva. A, Time-lapse, 3D dual-color SLAM imaging of a moving L2 stage transgenic *C. elegans* is imaged using ~4 μm laser light-sheet illumination and 20×/0.45NA objective. The GFP (GCaMP) and RFP (wCherry) two channel signals are obtained simultaneously by a single sCMOS camera (Hamamatsu, Flash 4.0 V3) combined with an image splitter (Hamamatsu, W-view GEMINI). The plane images are acquired at 200 frames per second. Each worm is recorded for 12 seconds, generating ~20 consecutive SLAM volumes. B, Time-lapsed volume rendering sequence (6 of 20) that visualizes the behaving worm in full size and real time. C, Vignette high-resolution views of 6-second time point with *x-y*, *x-z* projections, and volume rendering shown, respectively. The imaging volume is 665.6 × 166.4 × 128 $\mu m^3$, with 0.325 × 0.325 × 1.5 $\mu m^3$ voxel size. D, The correlation between muscle-bending curvature (ventral and dorsal) with that of $Ca^{2+}$ signal variation. Muscle contractions induced curvature changes have relatively high correlation coefficients with the fluctuation of local $Ca^{2+}$ signals. Scale bars are 100 μm. GFP, green fluorescent protein; SLAM, sub-voxel-resolving light-sheet add-on microscopy

NA detection, ~4 μm light-sheet illumination, and continuous volumetric sectioning of the entire animal at ~1.7 dual-color volumes per second. For each sample, recording lasted at least 12 seconds during which over 20 image volumes were acquired (Figure 6A). Fluctuation of GCaMP6 fluorescence signal intensity, normalized against that of Cherry signals, was extracted to quantify changes in the muscle activity.

As shown in six consecutive rendered imaging volumes (Figure 6B,C), acquired images are capable of resolving the time-varying $Ca^{2+}$ signal changes of the entire worm (Figure S12). As shown in Figure 6D, degree

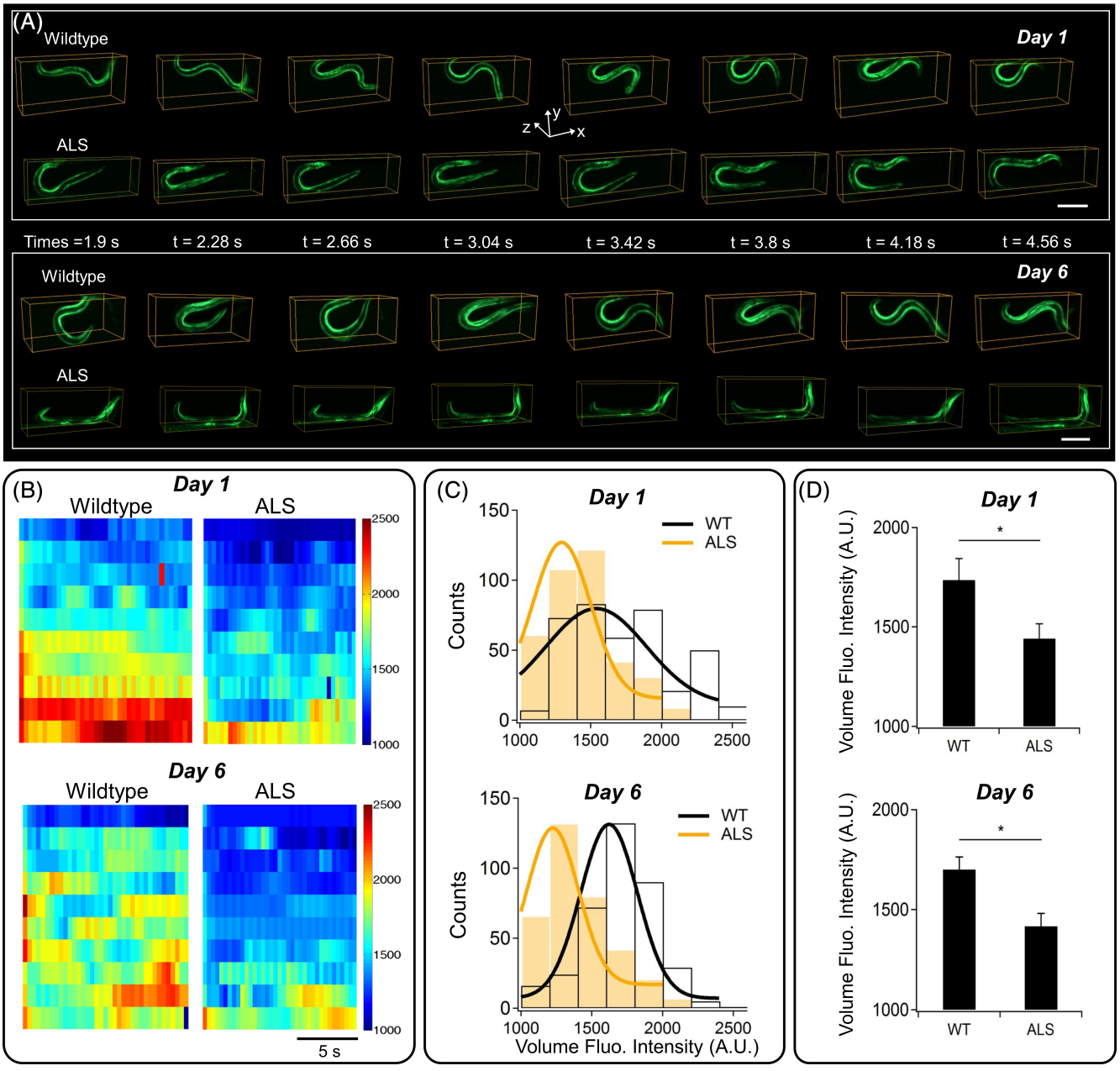


**FIGURE 7** Comparison of muscle calcium activities between age-matched wildtype and amyotrophic lateral sclerosis (ALS) models of *C. elegans*. A, Serial SLAM volumetric reconstructions of wildtype and ALS *C. elegans* model (FUS501) at adult day 1 and day 6, respectively. GCaMP6 fluorescence signals are acquired at ~3 volumes per second, sufficient to capture the dynamic changes that correlated with muscle contraction in locomoting animals. The 37 volumes continuously captured in 14 seconds with ~0.38 second interval are shown in Video S2 and S3. B, The fluorescence intensity heatmap illustrates the dynamic changes of each wildtype and ALS animals (n = 10 for each group). C, Histograms of full volume fluorescence intensity in age-matched wildtype and ALS animal samples. Gaussian-fitting curves approximate intensity distributions. At day 6, the shift of the Gaussian-fitting curve is larger than at day 1. D, The averaged volume fluorescence intensity of wildtype and ALS model in day 1 and day 6, respectively. Scale bars, 300 μm. SLAM, sub-voxel-resolving light-sheet add-on microscopy

of the muscle bending (counted as body local curvature) was correlated with local $Ca^{2+}$ signal variations (counted as GFP/RFP ratio), consistent with the notion that muscle activation causes contraction (Figure 6D). Thus, with this SLAM device, a conventional microscope gains the capability of functional volumetric imaging of small-sized and moving animals.

### 2.8 | Detecting cellular activity difference in an amyotrophic lateral sclerosis animal model by SLAM

To determine if SLAM imaging analyses can reveal quantifiable difference across samples, we compared muscle activities between wildtype *C. elegans* and an amyotrophic lateral sclerosis (ALS) *C. elegans* model FUS501. ALS is a fatal neurodegenerative disorder. FUS is an RNA-binding protein, where pathological mutations have been identified in a fraction of ALS patients [42, 43]. A transgenic *C. elegans* strain that ectopically expresses FUS with a small C-terminal truncation (FUS501), has been used to examine the model the physiological effect of the pathological form of FUS, including the changes on protein's aggregation property and subcellular location, as well as mobility [44, 45]. Indeed, we confirmed FUS501-expressing animals exhibited significantly reduced bending frequency when compared to that of wildtype animals, most prominently at aged adults (Figure S13), indicating a muscle activity loss in aged adults.

We are curious whether SLAM could reveal the muscle activity difference between two strains. We recorded age-matched day 1 and day 6 FUS501 and wildtype *C. elegans* adults. Each group included 10 samples; each sample was imaged for ~14 seconds at ~2.6 volume per second, acquiring 37 volumes in total (Videos S4 and S5). Following SVR and image rendering, the GCaMP6s signal change was extracted and compared. For quantification, the mean value of GCaMP signal change during each imaging volume (shown as a heat map in Figure 7B) was used as indexes for overall muscular activity at such a time interval for each recorded animal. Histogram of the intensity during the recording period pooled from all samples in each group was plotted with Gaussian fitting (Figure 7C), and the mean value of total signal changes of all samples and during the entire recording period was plotted for each group (Figure 7D). In both day 1 and day 6 old adults, the ALS (FUS501) animal models exhibited reduced signals when compared to wildtype animals. These results are consistent with a reduced motility of ALS (FUS501) adults to age-matched wildtype adults (Figure S13) [46, 47].

## 3 | CONCLUSION

We report here a simple, efficient, and powerful approach for advanced light-sheet imaging on a conventional microscope, SLAM. In addition to the immediate contrast and axial resolution enhancement by introducing sharp plane illumination, the continuous sub-voxel-scanning mode allows for rapid acquisition of shift-modulated images at a rate up to hundreds of frames per second. Finally, 3D resolution enhancement is achieved by applying probability-based SVR algorithm to acquired images, a procedure that isotropically improves the numerical aperture of the light-sheet images over twofold. Together, SLAM results in resolution enhancement over 10 times to original epifluorescence images.

We applied SLAM to image biological samples and phenomena of vastly different sizes and frequency. From the revealing the heartbeat and vessel structure of live zebrafish embryos, the muscle activities of behaving *C. elegans*, to neural anatomy of a cleared mouse brain, the resolution of SLAM was comparable to those obtained with benchtop light-sheet modalities. Its ability to upgrade a conventional wide-field microscope to achieve high-speed, multidimensional imaging of specimens with scalable space-bandwidth product renders SLAM a powerful tool for broad biological applications. SLAM's compact and add-on format allows most microscopes in service to perform light-sheet imaging at an affordable expense. Lastly, SLAM's open design allows easy combination with other modules, such as the dual-side illumination and multi-view functions, per evolving biological demands.

## 4 | EXPERIMENTAL SECTION

### 4.1 | Sample manipulation for SLAM experiment

Live samples, such as trans-genetic zebrafish embryo and *C. elegans*, were mounted on a thin, transparent FEP slide (0.5 mm thickness, Taobao, China) using agarose solution (low melt-point, 0.5%-1%). A micro-channel was engraved on the slide to confine the behaving worm inside the FOV of microscope. Then the prepared sample slide was clamped on the wedge-shaped adapter, thereafter being sucked to the holder by magnetism. As illustrated in Figure 1F, neither the illumination laser nor the emitted signals transmit through the FEP slide so that no optical artifacts or aberrations from the FEP slide influence the image quality. For imaging excised mouse brain, chemical clearing was implemented beforehand to

minimize the tissue scattering. We used an organic-solvent-based clearing method (uDISCO) to clarify the brain of a 8-week transgenic adult mouse that was labeled with Thy 1-green fluorescent protein (line M, Jackson Laboratory). The picture of cleared brain tissue was shown in Figure 5A. Two set screws were in this case used to clamp the cleared-and-harden mouse brain (also see Figure S2F, 2) and dip it in the glass chamber which was filled with refractive index-matched solvent (benzyl alcohol + benzyl benzoate + diphenyl ether, BABB-D).

## 4.2 | Off-*z*-axis scanning for SVR reconstruction

Unlike conventional stepwise *z*-scan applied in 3D microscopy, in SLAM-SVR mode, the samples were continuously moved along a vector with 78° angles with respect to the *x* and *y* directions of the camera pixel grid. Also based off the Nyquist sampling that is often used, SLAM scanned the samples through the laser light-sheet with a sampling step-size significantly smaller than the light-sheet thickness, and hence created nanoscale shift components simultaneously in both lateral and axial directions through a simple 1D motion. The unconventional off-*z*-axis scanning mode in conjunction with ultra-small step-size encrypted subtle lateral and axial shifts into the raw SLAM image stack. As a reference point, for SLAM-SVR imaging of the zebrafish whole embryo, the sample was scanned through the laser light-sheet with a 230 nm step-size, resulting an incremental lateral and axial shift of ~34 and 225 nm. A low magnification detection objective (4×/0.16, Olympus) was used to cover the entire large sample, and a sCMOS camera was used to continuously record the fluorescence images at high speed of 100 fps. The data acquisition time of sub-voxel scanning was only 35 seconds for zebrafish embryo (3500 frames in total). Then the recorded plane images were transferred from the camera to a RAID 0 array of two solid state drives. Finally, 48 groups of LR, 3D images were extracted from the raw image stack to compute the SVR image. A table that sorts the SLAM imaging parameters (axial extent of sectioning, step-size, acquisition speed, reconstruction speed, etc) for all the demonstrated samples under different modes is further shown as Table. S2. The current design of SLAM works with an inverted conventional microscope, so it only fits the air objectives with working distance greater than 3 mm and does not support the use of liquid immersion objective. A SLAM designed with an upright microscope in future could avoid the glass between the objective and sample and allow the use of immersion objective.

Taking the camera under-sampling into account, the effective lateral and axial resolution of each LR fish image are limited, being ~4 and 12 μm, respectively, with yielding ~200 megavoxel SBP over a ~2 $mm^3$ volume. After modeling the LR image sets with known shifts, optical aberration and digital decimation, the SVR image containing 10 gigavoxels could be obtained by iteratively seeking a HR solution which has maximum likelihood to the sum of the LR measurements after serial degradations being applied [36]. With handling the generated sub-voxel spatial shifts, the SVR procedure estimates the super-resolved 3D output that best suits a certain conditional probability in spatial domain, and computationally increases the SBP which is originally clamped by the physical limitations of system optics. It should be noted that without the incomplete sampling or shifting, the SVR method would have the same limits as deconvolution. Therefore, the algorithm is better suited to fluorescent imaging of large specimens, for which a large field-of-view is required and the recorded digital images are generally under-sampled. Our GPU-based SVR procedure is exactly developed for such large-scale computation, being fast with over two-orders acceleration as compared to traditional CPU-based computation. By the use of two NVidia GTX 2080ti graphical cards, the processing time of abovementioned zebrafish embryo was dramatically reduced from 2 hours to around 1 minute. The speed can be easily improved by using more GPUs.

## 4.3 | Dual-color SLAM imaging of live dynamics

By using a high-speed actuator, we scanned the behaving *C. elegans* through a dual-color laser light-sheet (488 and 590 nm) back and forth rapidly (0.3 mm/s). The sample was optically sectioned with a step-size of 1.5 "μm" and three-dimensionally imaged at both its forward and backward states with a short exposure of 5 ms and maximum acquisition rate of ~200 frames per second. We used an image splitter (Hamamatsu W-VIEW GEMINI, A82101-01) to simultaneously image dual-channel fluorescent signals onto a single sCMOS camera (Hamamatsu Flash 4.0 V3). After the mixed fluorescence going through the splitter, the GFP signals were projected onto the upper half of the sensor while the wCherry signals were directed to the lower half (Figure S1). Therefore, we were able to obtain dual-channel images with one capture. The consecutively acquired time-lapsed, dual-color image volumes ("665.6 μm × 166.4 μm × 128 μm" in size) can be furthermore translated into five-dimensional

visualization via reversing the images captured at backward state and merging the two channels.

## 4.4 | Zebrafish embryo culture

Adult Tg(*fli1a*:*EGFP*) and Tg(*cmlc2*:*GFP-Gata1*:*DsRed*) transgenic zebrafish were raised in the zebrafish core facility of Huazhong University of Science and Technology (HUST). All the experiments were performed in compliance with the approval of GLA Institutional Animal Care and Use Committee (IACUC) protocol (Zebrafish IACUC Protocol number: 101004-14). The zebrafish maintained with filtered fresh water under 14 hours of incandescent light and 10 hours of dark conditions. In Tg(*fli1a*:*EGFP*) fish, the fli1a promoter-driven enhanced green fluorescent protein (EGFP) was expressed predominantly in vascular endothelial and endocardial cells. In Tg(*cmlc2*:*GFP*) fish, the *cmlc2* promoter-driven GFP was expressed exclusively in myocardia cells. The embryos incubated in 31°C with petri dish. To maintain transparency of zebrafish embryos, embryos were incubated with egg water containing 0.2 mM 1-phenyl-2-thio-urea (Sigma) to suppress pigmentation at 24 hpf. The live fish embryos are anesthetized with 0.04 mg/mL of tricaine (MS-222, Sigma) before they are mounted to the slide for sustained imaging.

## 4.5 | *C. elegans* preparation

All strains were maintained at 22°C on NGM plates with OP50 *E. coli* as food. The strains used in this study were: ZM5848: *hpIs237* [*psu006*::*GFP-fus(del501)*], ZM9140: hpIs600 [*Pmyo-3*::*GCaMP6*::*wCherry*], SGA45: hpIs237; hpIs600. In thrashing experiments, animals cultured 16 hours post L4 larva were scored as day 1 adults. Individual animals were transferred into 5 μL of M9 buffer on a glass slide. Thirty seconds after the transfer, the frequency of the body bending was counted for 1 minute [44]. A single thrashing was defined as a complete sinusoidal movement through the head and tail. The same protocol was used to assess the motor function in day 6 adults.

## ACKNOWLEDGMENTS

We thank Haiwen Li for technical assistance, Yanyi Huang for discussions and comments on the manuscript. National Key R&D program of China (2017YFA0700501), Research Program of Shenzhen (JCYJ20160429182424047), the National Natural Science Foundation of China (21874052, 61860206009, 31871069, and 31671052), the National Science Foundation of Hubei (2018CFA039), Wuhan Morning Light Plan of Youth Science and Technology (2017050304010295), the Innovation Fund of WNLO, The Fundamental Research Funds for the Central Universities (2019kfyRCPY060, 2019JYCXJJ012), and the Junior Thousand Talents Program of China (P.F. and S.G.).

## CONFLICT OF INTEREST

The authors declare that there are no conflicts of interest related to this article.

## AUTHOR CONTRIBUTIONS

P.F. conceived the idea. P.F., S.G. oversaw the project. H.J., Y.Y., and X.X. developed the optical setups. H.Z. developed the programs. Y.L., T.Y., and H.J. conducted the sample preparation experiments. Y.Y., H.J., and Y.L., F.Z. conducted the experiments. H.Z., X.W., Q.L., F.Z., and P.F. processed the images. S.L., M.Z., S.G., D.Z., and P.F. analyzed the data and wrote the paper.

## DATA AVAILABILITY STATEMENT

Custom codes for SVR computation implemented in current study are available from the corresponding authors upon request.

## ORCID

*Peng Fei* https://orcid.org/0000-0003-3764-817X

## REFERENCES

[1] J. Huisken, J. Swoger, F. Del Bene, J. Wittbrodt, E. H. K. Stelzer, *Science* **2004**, *305*, 1007.
[2] P. J. Keller, A. D. Schmidt, J. Wittbrodt, E. H. K. Stelzer, *Science* **2008**, *322*, 1065.
[3] T. A. Planchon, L. Gao, D. E. Milkie, M. W. Davidson, J. A. Galbraith, C. G. Galbraith, E. Betzig, *Nat. Methods* **2011**, *8*, 417.
[4] E. G. Reynaud, U. Krzic, K. Greger, E. H. Stelzer, *HFSP J.* **2008**, *2*, 266.
[5] M. Mickoleit, B. Schmid, M. Weber, F. O. Fahrbach, S. Hombach, S. Reischauer, J. J. N. M. Huisken, *Nat. Methods* **2014**, *11*, 919.
[6] Y. Wu, P. Wawrzusin, J. Senseney, R. S. Fischer, R. Christensen, A. Santella, A. G. York, P. W. Winter, C. M. Waterman, Z. Bao, D. A. Colon-Ramos, M. McAuliffe, H. Shroff, *Nat. Biotechnol.* **2013**, *31*, 1032.
[7] M. B. Ahrens, M. B. Orger, D. N. Robson, J. M. Li, P. J. Keller, *Nat. Methods* **2013**, *10*, 413.
[8] T. Breuninger, K. Greger, E. H. K. Stelzer, *Opt. Lett.* **2007**, *32*, 1938.
[9] B. C. Chen, W. R. Legant, K. Wang, L. Shao, D. E. Milkie, M. W. Davidson, C. Janetopoulos, X. S. Wu, J. A. Hammer, Z. Liu, B. P. English, Y. Mimori-Kiyosue, D. P. Romero, A. T. Ritter, J. Lippincott-Schwartz, L. Fritz-Laylin, R. D. Mullins, D. M. Mitchell, J. N. Bembenek, A.-C. Reymann, R. Böhme, S. W. Grill, J. T. Wang, G. Seydoux, U. S. Tulu, D. P. Kiehart, E. Betzig, *Science* **2014**, *346*, 1257998.
[10] C. J. Engelbrecht, K. Greger, E. G. Reynaud, U. Kržic, J. Colombelli, E. H. K. Stelzer, *Opt. Express* **2007**, *15*, 6420.

[11] C. J. Engelbrecht, E. H. Stelzer, *Opt. Lett.* **2006**, *31*, 1477.
[12] J. Huisken, D. Y. R. Stainier, *Development* **2009**, *136*, 1963.
[13] B. Schmid, G. Shah, N. Scherf, M. Weber, K. Thierbach, C. P. Campos, I. Roeder, P. Aanstad, J. Huisken, *Nat. Commun.* **2013**, *4*, 2207.
[14] T. F. Holekamp, D. Turaga, T. E. Holy, *Neuron* **2008**, *57*, 661.
[15] J. Huisken, D. Y. R. Stainier, *Opt. Lett.* **2007**, *32*, 2608.
[16] J. G. Ritter, R. Veith, J. Siebrasse, U. Kubitscheck, *Opt. Exp. Dermatol.* **2008**, *16*, 7142.
[17] J. Swoger, P. Verveer, K. Greger, J. Huisken, E. H. K. Stelzer, *Opt. Express* **2007**, *15*, 8029.
[18] D. Turaga, T. E. Holy, *Opt. Lett.* **2008**, *33*, 2302.
[19] P. J. Verveer, J. Swoger, F. Pampaloni, K. Greger, M. Marcello, E. H. K. Stelzer, *Nat. Methods* **2007**, *4*, 311.
[20] P. J. Keller, A. D. Schmidt, J. Wittbrodt, E. H. K. Stelzer, *Cold Spring Harb. Protoc.* **2011**, *2011*, 1235.
[21] H. U. Dodt, U. Leischner, A. Schierloh, N. Jährling, C. P. Mauch, K. Deininger, J. M. Deussing, M. Eder, W. Zieglgänsberger, K. Becker, *Nat. Methods* **2007**, *4*, 331.
[22] L. Gao, L. Shao, B.-C. Chen, E. Betzig, *Nat. Protoc.* **2014**, *9*, 1083.
[23] A. Kumar, Y. Wu, R. Christensen, P. Chandris, H. Shroff, *Nat. Protoc.* **2014**, *9*, 2555.
[24] A. K. Glaser, N. P. Reder, Y. Chen, E. F. McCarty, C. Yin, L. Wei, Y. Wang, L. D. True, J. T. C. Liu, *Nat. Biomed. Eng.* **2017**, *1*, 0084.
[25] R. Mcgorty, H. Liu, D. Kamiyama, Z. Dong, S. Guo, B. Huang, *Opt. Express* **2015**, *23*, 16142.
[26] P. G. Pitrone, J. Schindelin, L. Stuyvenberg, S. Preibisch, M. Weber, K. W. Eliceiri, J. Huisken, P. Tomancak, *Nat. Methods* **2013**, *10*, 598.
[27] C. S. Chard, P. Nec, V. Bertrand, P.-F. Lenne, Ois, *J. Vis. Exp.* **2014**, *87*, e51342.
[28] E. J. Gualda, H. Pereira, T. Vale, M. F. Estrada, C. Brito, N. Moreno, *Biomed. Opt. Express* **2015**, *6*, 4447.
[29] H. Deschout, K. Raemdonck, S. Stremersch, P. Maoddi, G. Mernier, P. Renaud, S. Jiguet, A. Hendrix, M. Bracke, R. Van den Broecke, M. Roding, M. Rudemo, J. Demeester, S. C. De Smedt, F. Strubbe, K. Neyts, K. Braeckmans, *Nanoscale* **2014**, *6*, 1741.
[30] P. Paie, F. Bragheri, A. Bassi, R. Osellame, *Lab Chip* **2016**, *16*, 1556.
[31] R. Regmi, K. Mohan, P. P. Mondal, *AIP Adv.* **2014**, *4*, 097125.
[32] J. Wu, R. K. Y. Chan, *Opt. Express* **2013**, *21*, 23921.
[33] T. Bruns, S. Schickinger, R. Wittig, H. Schneckenburger, *J. Biomed. Opt.* **2012**, *17*, 101518.
[34] T. C. Fadero, T. M. Gerbich, K. Rana, A. Suzuki, M. DiSalvo, K. N. Schaefer, J. K. Heppert, T. Boothby, B. Goldstein, M. Peifer, N. Allbritton, A. S. Gladfelter, A. S. Maddox, P. Maddox, *J. Cell Biol.* **2018**, *217*, 1869.
[35] Z. Guan, J. Lee, H. Jiang, S. Dong, N. Jen, T. Hsiai, C.-M. Ho, P. Fei, *Opt. Express* **2016**, *7*, 194.
[36] P. Fei, J. Nie, J. Lee, Y. Ding, S. Li, Z. Yu, H. Zhang, M. Hagiwara, T. Yu, T. Segura, C.-M. Ho, D. Zhu, T. K. Hsiai, *Adv. Photon.* **2019**, *1*, 13.
[37] J. Nie, S. Liu, T. Yu, Y. Li, J. Ping, P. Wan, F. Zhao, Y. Huang, W. Mei, S. Zeng, D. Zhu, P. Fei, *Adv. Sci.* **2019**, *7*.
[38] G. Zheng, R. Horstmeyer, C. Yang, *Nat. Photon.* **2013**, *7*, 739.
[39] J. F. Wendt, *Comput. Phys.* **1992**, *7*.
[40] W. L. Oberkampf, T. G. Trucano, *Adv. Mech.* **2007**, *38*, 209.
[41] C. Pan, R. Cai, F. P. Quacquarelli, A. Ghasemigharagoz, A. Lourbopoulos, P. Matryba, N. Plesnila, M. Dichgans, F. Hellal, A. Ertürk, *Nat. Methods* **2016**, *13*, 859.
[42] V. V. Belzil, J. St-Onge, H. Daoud, A. Desjarlais, J.-P. Bouchard, N. Dupré, W. Camu, P. A. Dion, G. A. Rouleau, *J. Hum. Genet.* **2011**, *56*, 247.
[43] M. DeJesus-Hernandez, J. Kocerha, N. Finch, R. Crook, M. Baker, P. Desaro, A. Johnston, N. Rutherford, A. Wojtas, K. Kennelly, Z. K. Wszolek, N. Graff-Radford, K. Boylan, R. Rademakers, *Hum. Mutat.* **2010**, *31*, E1377.
[44] T. Murakami, S.-P. Yang, L. Xie, T. Kawano, D. Fu, A. Mukai, C. Bohm, F. Chen, J. Robertson, H. Suzuki, G. G. Tartaglia, M. Vendruscolo, G. S. K. Schierle, F. T. S. Chan, A. Moloney, D. Crowther, C. F. Kaminski, M. Zhen, P. S. George-Hyslop, *Hum. Mol. Genet* **2012**, *21*, 1.
[45] T. Murakami, S. Qamar, J. Q. Lin, G. S. Schierle, E. Rees, A. Miyashita, A. R. Costa, R. B. Dodd, F. T. Chan, C. H. Michel, D. Kronenberg-Versteeg, Y. Li, S. P. Yang, Y. Wakutani, W. Meadows, R. R. Ferry, L. Dong, G. G. Tartaglia, G. Favrin, W. L. Lin, D. W. Dickson, M. Zhen, D. Ron, G. Schmitt-Ulms, P. E. Fraser, N. A. Shneider, C. Holt, M. Vendruscolo, C. F. Kaminski, P. St George-Hyslop, *Neuron* **2015**, *88*, 678.
[46] S. Brenner, *Genetics* **1974**, *77*, 71.
[47] S. Gao, M. Zhen, *Proc. Natl. Acad. Sci. U. S. A.* **2011**, *108*, 2557.

## SUPPORTING INFORMATION

Additional supporting information may be found online in the Supporting Information section at the end of this article.

**How to cite this article:** Zhao F, Yang Y, Li Y, et al. Efficient and cost-effective 3D cellular imaging by sub-voxel-resolving light-sheet add-on microscopy. *J. Biophotonics*. 2020;13:e201960243. https://doi.org/10.1002/jbio.201960243